

Postprint of: Kamatchi S., Ficek M., Kalpataru P., Yeh C., Mirosław S., Ryl J., Leou K., Young Park J., Lin I., Bogdanowicz R., Haenen K., Boron doped Nanocrystalline Diamond-Carbon Nanospire Hybrid Electron Emission Source, ACS Applied Materials & Interfaces, Vol. 11, No 51 (2019), pp. 48612-48623, DOI: [10.1021/acsami.9b17942](https://doi.org/10.1021/acsami.9b17942)

## Boron doped Nanocrystalline Diamond–Carbon Nanospire Hybrid Electron Emission Source

Kamatchi Jothiramalingam Sankaran,<sup>\*,†,‡,#</sup> Mateusz Ficek,<sup>§,#</sup> Kalpataru Panda,<sup>¶,€</sup> Chien-Jui Yeh,<sup>¥</sup> Mirosław Sawczak,<sup>⊥</sup> Jacek Ryl,<sup>||</sup> Keh-Chyang Leou,<sup>¥</sup> Jeong Young Park,<sup>¶,€</sup> I-Nan Lin,<sup>£</sup> Robert Bogdanowicz,<sup>§</sup> and Ken Haenen<sup>\*,†,‡</sup>

<sup>†</sup>Institute for Materials Research (IMO), Hasselt University, 3590 Diepenbeek, Belgium. Email: [sankaran.kamatchi@uhasselt.be](mailto:sankaran.kamatchi@uhasselt.be); [ken.haenen@uhasselt.be](mailto:ken.haenen@uhasselt.be)

<sup>‡</sup>IMOMECA, IMEC vzw, 3590 Diepenbeek, Belgium.

<sup>§</sup>Department of Metrology and Optoelectronics, Faculty of Electronics, Telecommunications and Informatics, Gdansk University of Technology, 11/12 G. Narutowicza St., 80-233 Gdansk, Poland.

<sup>¶</sup>Center for Nanomaterials and Chemical Reactions, Institute for Basic Science (IBS), Daejeon, 34141 Korea.

<sup>€</sup>Department of Chemistry, Korea Advanced Institute of Science and Technology (KAIST), Daejeon, 34141 Korea.

<sup>¥</sup>Department of Engineering and System Science, National Tsing Hua University, Hsinchu, 30013 Taiwan, Republic of China.

<sup>⊥</sup>Center for Plasma and Laser Engineering, The Szwedowski Institute of Fluid Flow Machinery, Polish Academy of Sciences, Fiszerka 14, 80-231 Gdansk, Poland.

<sup>||</sup> Department of Electrochemistry, Corrosion and Materials Engineering, Faculty of Chemistry, Gdansk University of Technology, Narutowicza 11/12, 80-233 Gdansk, Poland.

<sup>£</sup>Department of Physics, Tamkang University, Tamsui, 251 Taiwan, Republic of China.

<sup>#</sup>These authors contributed equally to this work.

**ABSTRACT:** Electron emission signifies an important mechanism facilitating the enlargement of devices that have modernized large parts of science and technology. Today, the search for innovative electron emission devices for imaging, sensing, electronics, and high-energy physics continues. Integrating two materials with dissimilar electronic properties into a hybrid material is an extremely sought-after synergistic approach envisioning a superior field electron emission (FEE) material. An innovation is described regarding the fabrication of a nanostructured carbon hybrid resulting from the one-step growth of boron doped nanocrystalline diamond (BNCD) and carbon nanospikes (CNSs) by a microwave plasma enhanced chemical vapor deposition technique. Spectroscopic and microscopic tools are used to investigate the morphological, bonding, and microstructural characteristics related to the growth mechanism of these hybrids. Utilizing the benefits of both the sharp edges of the CNSs and the high stability of BNCD, a promising FEE performance with a lower turn-on field of  $1.3 \text{ V } \mu\text{m}^{-1}$ , a higher field enhancement factor of 6780, and a stable FEE current stability lasting for 780 min is obtained. The microplasma devices utilizing these hybrids as a cathode illustrate a superior plasma illumination behavior. Such hybrid carbon nanostructures, with superb electron emission characteristics, can encourage the enlargement of several electron emission device technologies.

**KEYWORDS:** nanocrystalline diamond, carbon nanospike, one-step growth, field electron emission, microplasma illumination

---

## ■ INTRODUCTION

Modernization of novel electron sources is essential for numerous applications comprising integrated flat panel displays, electron guns, vacuum microelectronics, X-ray sources, and energy conversion devices. Field electron emission (FEE) based electron sources, specifically “cold-

1  
2  
3 cathodes”, are replacing conventional thermionic electron emission sources. FEE, also well-  
4  
5 known as Fowler-Nordheim (F-N) tunneling,<sup>1</sup> follows a quantum tunneling mechanism, where  
6  
7 under an external electric field electrons pass from a material’s surface into a vacuum. For  
8  
9 choosing a suitable material as an effective field emitter cathode, numerous standards such as  
10  
11 high chemical and mechanical stability, vacuum compatibility, electron affinity, resistance to  
12  
13 poisoning due to residual gases and ion bombardment, are considered.  
14  
15

16  
17 Owing to the fact that physical and geometrical parameters are greatly responsible for the  
18  
19 electron tunneling characteristics, one dimensional (1D) nanostructures for example nanotubes,  
20  
21 nanowires and nanorods have been deliberated as favorable emitter materials for FEE devices.  
22  
23 As overcoming the disadvantages of bulk device technologies, 1D nanostructures have quicker  
24  
25 device turn-on time, sustainability and compactness. Additionally, long and sharp nanoneedles  
26  
27 pointing in the various directions of these nanostructures are promising for improving the FEE  
28  
29 current density. A myriad of nanostructures from metals, semiconductors, and carbon materials  
30  
31 has been developed in an attempt to achieve better FEE performance, including Ge, Cu and Au  
32  
33 nanowires, SiC nanoparticles, PrB<sub>6</sub> nanorods, WS<sub>2</sub> nanotubes, ZnO nanowalls, graphene  
34  
35 nanoedges, boron nanosheets, carbon nanotubes, diamond nanorods, and many others.<sup>2–11</sup>  
36  
37 Compared to metals and semiconductors, carbon nanostructures such as carbon nanotubes,  
38  
39 carbon nanosheets, nanodiamonds, and graphene show enhanced FEE characteristics.<sup>12</sup>  
40  
41  
42  
43

44  
45 Generally, materials with outstanding FEE characteristics display a low turn-on field,  
46  
47 high current density, large field enhancement factor, high stability, and long lifetime. But it is  
48  
49 very hard to discover these characteristics in a single material. For example, along with sharp  
50  
51 edges and high aspect ratio, CNTs and graphene create a low turn-on field, high current density,  
52  
53 and high field enhancement factor. Nevertheless, these materials face the challenges of  
54  
55

1  
2  
3 insufficient device lifetime and long-term emission stability.<sup>13,14</sup> The FEE properties of these  
4 materials are degraded because the residual gases in the FEE devices damage the sharp edges of  
5 these materials after a long-time ion bombardment. On the other hand, because of its strong  
6 bonding structure, diamond shows better lifetime stability and reliability, but its intrinsic  
7 insulating nature results in a high turn-on field and low current density. Consequently,  
8 combining different nanoscale carbon materials to synthesize a hybrid material is considered to  
9 be an effective route to achieve enhanced FEE characteristics compared with a single  
10 nanocarbon material. Varshney *et al.* have fabricated a layered graphene-diamond hybrid that  
11 achieves a turn-on field of  $3.8 \text{ V } \mu\text{m}^{-1}$  and a long-lasting stable FEE current of 0.1 mA over 135  
12 h.<sup>15</sup> CNTs-carbon nanoflake hybrid balls with a low turn-on field of  $1.77 \text{ V } \mu\text{m}^{-1}$  was  
13 successfully synthesized by Chang *et al.*<sup>16</sup> Microcrystalline diamond/CNT double-layered  
14 pyramid arrays acquire a low turn-on field of  $2.84 \text{ V } \mu\text{m}^{-1}$  and a long lifetime above 100 h.<sup>17</sup>  
15 Chang *et al.* have coated nitrogen doped diamond on CNTs that display a low turn-on field of  
16  $3.58 \text{ V}/\mu\text{m}$  and noticeably improved the robustness of CNTs.<sup>18</sup> Yuge *et al.* described a low turn-  
17 on field of  $12 \text{ kV cm}^{-1}$  for single-walled CNTs grown on single-walled carbon nanohorn  
18 aggregates.<sup>19</sup> Graphene/carbon nanofilament hybrids illustrate a low turn-on field of  $1.34 \text{ V } \mu\text{m}^{-1}$   
19 and a high field enhancement factor of 4930, which were reported by Dai *et al.*<sup>20</sup> Xiao *et al.*  
20 developed an ultrananocrystalline diamond (UNCD)-carbon nanofiber hybrid field emitter with a  
21 low threshold field emission of  $2.5 \text{ V}/\mu\text{m}$ .<sup>21</sup> FEE tests of microstructured diamond  
22 films/vertically aligned multiwalled CNT reveal a low threshold voltages of  $2 \text{ V } \mu\text{m}^{-1}$  with  
23 longer lifetime stability up to 35 h<sup>22</sup> and 75 h.<sup>23</sup> Uppireddi *et al.* synthesized hybrid films  
24 comprising microstructured diamond films-carbon nanostructures, which showed low turn-on  
25 field of  $2.5 \text{ V}/\mu\text{m}$  and good temporal stability over a period of 24 h.<sup>24</sup> Hybrid graphene-CNT  
26  
27  
28  
29  
30  
31  
32  
33  
34  
35  
36  
37  
38  
39  
40  
41  
42  
43  
44  
45  
46  
47  
48  
49  
50  
51  
52  
53  
54  
55  
56  
57  
58  
59  
60

1  
2  
3 field emitters reported by Koh *et al.*<sup>25</sup> and Liu *et al.*<sup>26</sup> shows lower turn-on field, which is  
4 ascribed to the enhanced electrical conductivity and field enhancing emission spots on the  
5 surface of the graphene sheet. Also, a hybrid film with a reduced graphene oxide-CNT reveals a  
6 low turn on field and threshold field of 2.82 and 3.00 V/ $\mu\text{m}$ .<sup>27</sup> Catalytically synthesized few-  
7 layer graphene on vertically aligned diamond nanorods shows a low turn-on field of 4.21 V/ $\mu\text{m}$   
8 and a large field enhancement factor of 3480.<sup>28</sup> However, a multi-step growth process is involved  
9 in fabricating these hybrids materials, which are technologically complicated and more  
10 economically unfavored.  
11  
12  
13  
14  
15  
16  
17  
18  
19  
20

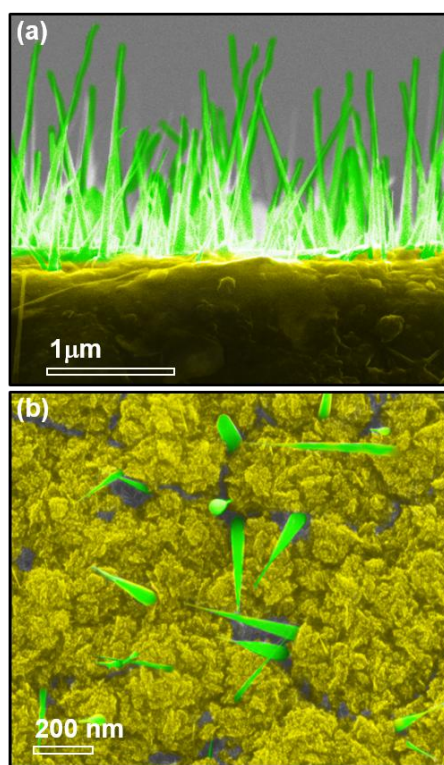
21 In this work, a direct one-step microwave plasma enhanced chemical vapor deposition  
22 (MPECVD) synthesis of boron doped nanocrystalline diamond (BNCD)-carbon nanospire  
23 (CNS) hybrids is presented, with CNS-on-BNCD as the key motivation. The BNCD-CNS  
24 hybrids are outstanding field electron emitters with all of the preferred characteristics, such as  
25 low turn-on field, high field enhancement factor, and prolonged emission stability, which are  
26 superior to those of other kinds of hybrids reported earlier. Atomic force microscopy (AFM)-  
27 based peak forced-tunneling atomic force microscopy (PF-TUNA) technique was used to  
28 directly explore the local electron emission sites from these hybrids. Moreover, the potential  
29 applications of these superior FEE hybrid materials as microplasma cathodic devices were  
30 demonstrated.  
31  
32  
33  
34  
35  
36  
37  
38  
39  
40  
41  
42  
43

## 44 ■ RESULTS AND DISCUSSION

### 45 **Material's characteristics**

46  
47 Scanning electron microscopy (SEM) was employed to examine the BNCD-CNS hybrids. The  
48 cross-sectional SEM micrograph shown in Figure 1a reveals that 1D separated spike-shaped  
49 carbon nanostructures were grown directly on the BNCD films. The nanospikes are sharp,  
50  
51  
52  
53  
54  
55

1  
2  
3 vertically aligned and no branching was observed; they are distributed randomly on the whole  
4 surface of the BNCD films. The size of the CNSs was estimated to be ~50–100 nm in diameter  
5 and ~2  $\mu\text{m}$  in height. Figure 1b shows the plan-view SEM image which exhibits that the CNSs  
6 were protruding outside from the BNCD films and the BNCD films have 10–20 nm sized  
7 cauliflower-like grains with thickness around 1.2  $\mu\text{m}$ . Moreover, Figure S1a of supporting  
8 information displays the SEM micrograph of a thin layer of BNCD films grown directly on a  
9 silicon substrate in the first stage of the sample preparation. The thickness of thin BNCD films is  
10 around 170 nm, which is estimated from the cross-sectional SEM micrograph shown in Figure  
11 S1b, supporting information.  
12  
13  
14  
15  
16  
17  
18  
19  
20  
21  
22  
23  
24  
25  
26  
27  
28  
29  
30  
31  
32  
33  
34  
35  
36  
37  
38  
39  
40  
41  
42  
43  
44  
45  
46  
47  
48



49 **Figure 1.** (a) Cross-sectional SEM micrograph of BNCD-CNS hybrids and (b) the corresponding  
50 plan-view SEM micrograph. The SEM micrographs of BNCD samples after first phase of growth  
51 are presented in Figure S1, supporting information.  
52  
53  
54  
55  
56  
57  
58  
59  
60

1  
2  
3 Raman and X-ray photoelectron spectroscopy (XPS) measurements were accomplished  
4 to understand the chemical bonding states of the BNCD-CNS hybrids. The Raman spectrum  
5 shown in Figure 2a was recorded for a thin layer of BNCD grown directly on a silicon substrate  
6 in the first stage of the sample preparation. Except for the silicon bands at 520 and 960  $\text{cm}^{-1}$  the  
7 wide band with maximum around 1320  $\text{cm}^{-1}$  is observed, which is due to the nanocrystalline  
8 features of diamond grains in the BNCD films (cf. Figure 1b).<sup>19</sup> Generally, a sharp Raman peak  
9 at 1332  $\text{cm}^{-1}$  is observed for the diamond films with large grain sizes.<sup>13,28</sup> The  $\nu_1$  band at  $\sim 1130$   
10  $\text{cm}^{-1}$  reveals the presence of *trans*-polyacetylene phases at the grain boundaries.<sup>29</sup> The band at  
11 1550  $\text{cm}^{-1}$  represents the G band ( $sp^2$  carbon phase). The Raman spectrum recorded for the  
12 BNCD-CNS hybrids shown in Figure 2b is different from the Raman spectrum observed for the  
13 first stage of BNCD film growth (cf. Figure 2a). The spectrum is dominated by two intense  
14 bands: the D band centered near 1350  $\text{cm}^{-1}$  is initiated by the lattice disorder ensuing from the  
15 finite crystalline size and the G band centered near 1585  $\text{cm}^{-1}$  signifies the presence of  $E_{2g}$  mode  
16 of graphite,<sup>30</sup> respectively. The peak positions, full-width half maximum and intensities of the D  
17 and G bands, determined by fitting a Lorentzian distribution are listed in inset b<sub>1</sub> of Figure 2b.  
18 The  $I_D/I_G$  ratio for the investigated material is 1.06 which corresponds to a multiwalled carbon  
19 nanotube-like structure.<sup>31</sup> A second order 2D band arises around 2716  $\text{cm}^{-1}$  signifying the  
20 presence of nanographite and a D+G band at 2920  $\text{cm}^{-1}$  is due to defects at  $sp^2$  sites. Besides this,  
21 in the low wavenumber range, a wide asymmetric band with a maximum at 451  $\text{cm}^{-1}$  was  
22 noticed, indicating boron doped carbon materials originating in boron induced defects.  
23  
24  
25  
26  
27  
28  
29  
30  
31  
32  
33  
34  
35  
36  
37  
38  
39  
40  
41  
42  
43  
44  
45  
46  
47  
48  
49  
50  
51  
52  
53  
54  
55  
56  
57  
58  
59  
60

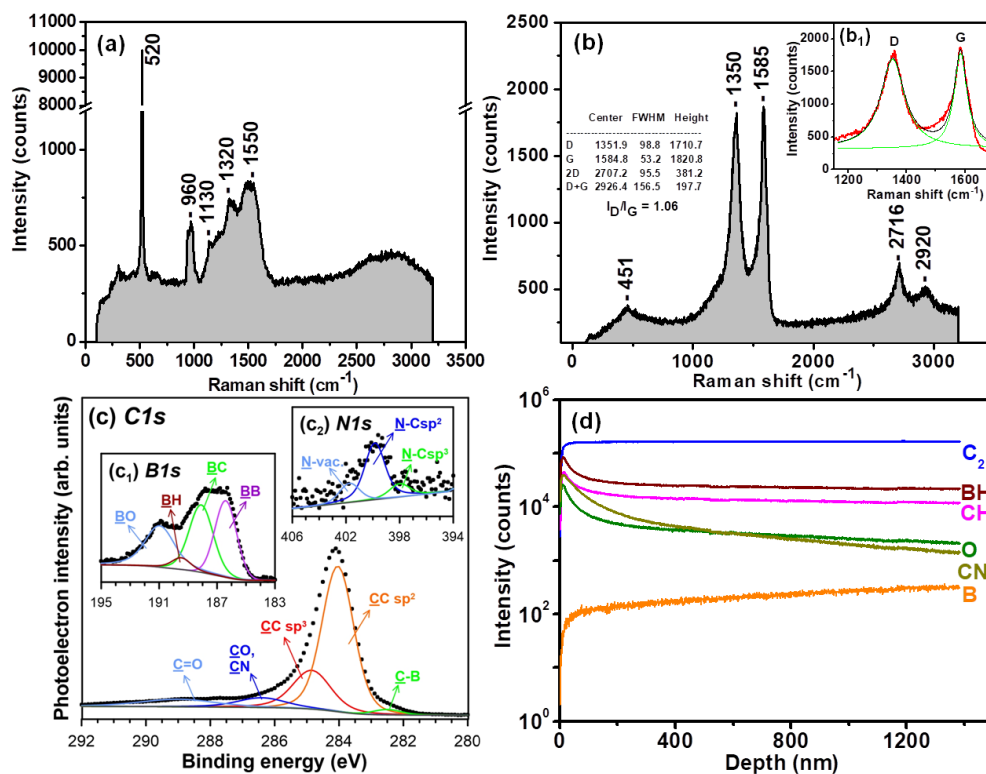


**Figure 2.** visible-Raman ( $\lambda = 514$  nm) spectra of (a) BNCD and (b) BNCD-CNS hybrids. The full-width half maximum and intensities of D and G bands of BNCD-CNS hybrids, determined by fitting with a Lorentzian distribution is shown in the inset  $b_1$ . (c)  $C1s$  XPS spectrum of BNCD-CNS hybrids along with  $B1s$  (inset “ $c_1$ ”) and  $N1s$  (inset “ $c_2$ ”) XPS spectra of the materials. (d) SIMS depth profile of the growth species such as  $C_2$ , BH, CH, CN, and B in the  $H_2/CH_4/B_2H_6/N_2$  plasma.

The XPS analysis was performed in the binding energy range characteristic for  $C1s$ ,  $B1s$  and  $N1s$ , as presented on Figure 2c. The dominant influence of carbon was revealed, with five individual components present in the  $C1s$  spectrum. Most notably, two peaks located at 284.0 and 284.8 eV are related to  $sp^2$ - and  $sp^3$ -carbon, respectively. The  $sp^2$ -to- $sp^3$  ratio, estimated on the base of XPS data analysis was found to be 2.9:1. Next, two carbon components were located



1  
2  
3 at more positive energies, corresponding to oxidized C-O and C-N bonds. The incorporation  
4 boron into a nanospike lattice is indicated by the appearance of a peak at 282.5 eV.<sup>32</sup> In the *B1s*  
5 region (inset *c*<sub>1</sub> of Figure 2c), the broad peak shape indicates the presence of multiple types of  
6 boron interactions. The majority of the absorption peaks are seen to be associated with elemental  
7 boron and B-C bonding energies.<sup>33</sup> The small contribution at 189.5 eV reveals the presence of B-  
8 H bonds. A similar interaction was previously observed in the case of borohydrides.<sup>34</sup> However,  
9 similar peak energies were reported for a boron atom substituted in the graphitic structure.<sup>35</sup>  
10 Next, the *B1s* peak value of 191.0 eV shows sign of boron oxidation in the analyzed sample. The  
11 presence of oxygen on the sample surface originated from exposure to atmosphere and its  
12 contribution did not exceed 5%, a value typical for air-exposed diamond-based electrodes.<sup>36</sup> On  
13 the other hand, inset *c*<sub>2</sub> of Figure 2c shows the deconvoluted *N1s* spectrum. The dominant  
14 component at 399.9 eV is ascribed to nitrogen atoms in *sp*<sup>2</sup>-carbon environment, while the  
15 component attributed to nitrogen atoms bonded with *sp*<sup>3</sup>-carbon is typically shifted to more  
16 negative binding energies, here at 398.0 eV. Their ratio corresponds *sp*<sup>2</sup>-to-*sp*<sup>3</sup> ratio obtained  
17 based on *C1s* spectrum deconvolution. Finally, the most positively charged nitrogen atoms  
18 originate from surface contamination with oxygen or nitrogen atoms trapped in vacancy defects  
19 created in the nitride layer. The deconvolution results are summarized in Table S1, Supporting  
20 Information. The induction of *sp*<sup>2</sup> phases in BNCD-CNS hybrids due to B and N doping  
21 discloses that doping of heteroatoms in carbon increases the graphitic nature as well as the  
22 electrical conductivity.<sup>37,38</sup> Furthermore, secondary ion mass spectroscopic (SIMS)  
23 measurements were carried out to confirm the elemental species assisting in the formation of  
24 BNCD-CNS hybrids. The SIMS depth profile of the growth species such as C<sub>2</sub>, BH, CH, CN,  
25 and B is displayed in Figure 2d, whereas the corresponding two-dimensional mapping is shown

1  
2  
3 in Figure S2. We clearly observed that the C<sub>2</sub> species possess a high intensity with high bright  
4 regions (Figure S2a). BH and CH species are almost at the same intensity followed by the CN, O  
5 and B species, which indicates a uniform distribution of these species throughout the thickness of  
6 the films. This is contradictory to the common observation that boron concentration is usually  
7 present at the surface rather than throughout the bulk of the material.<sup>39</sup> The SIMS depth profile is  
8 consistent with the observations from the XPS studies.  
9

## 17 **Potential Applications**

### 21 *Field Electron Emitters*

22  
23  
24 Various functional properties can be envisioned from these hybrid materials. Owing to their  
25 sharply pointed 1D nanospikes, these hybrids are anticipated to be an effective field electron  
26 emitter. Figure 3a shows the FEE plot of the current density ( $J_{\text{FEE}}$ ) as a function of the applied  
27 electric field ( $E$ ) for the BNCD-CNS hybrids with the schematic of the FEE measurement setup  
28 as inset. The turn-on field ( $E_0$ ) was evaluated by extrapolating two straight lines on both the  
29 lower and higher sides of the electric field in the F-N plot. Here,  $E_0$  is measured to be 1.3 V/ $\mu\text{m}$   
30 and a  $J_{\text{FEE}}$  value of 2.7 mA/cm<sup>2</sup> at  $E=2.0$  V/ $\mu\text{m}$ . It should be mentioned that we have tested five  
31 BNCD-CNS hybrids at three places of each sample in the same configuration at a constant  
32 cathode to anode distance. The FEE characteristics of these five BNCD-CNS hybrid-based  
33 cathodic devices were reproducible for three times without altering their emission properties  
34 ( $J_{\text{FEE}}-E$  characteristics).  
35  
36  
37  
38  
39  
40  
41  
42  
43  
44  
45  
46  
47  
48  
49

50 Generally, the FEE process from a material is modeled by the F-N model:<sup>1</sup>

$$52 \quad J_{\text{FEE}} = (A\beta^2 E^2 / \varphi) \exp(-B\varphi^{3/2} / \beta E)$$

1  
2  
3 where  $A=1.54 \times 10^{-6}$  A eV/V,  $B=6.83 \times 10^9$  eV<sup>-3/2</sup> V/m,  $\beta$  is the field-enhancement factor and  $\varphi$   
4 is the work function of the emitters, respectively,. The inset image of Figure 3a displays the F-N  
5 plot, viz.  $\ln(J_{FEE}/E^2)$  versus  $1/E$ , which fits well with a straight line, representing that the BNCD-  
6 CNS hybrids obey the F-N rule. The  $\beta$  value can be calculated from the slope of the fitted line  
7 using the following equation:  
8  
9  
10  
11  
12  
13

$$\beta = -6.8 \times 10^3 \times \varphi^{1.5} / m$$

14  
15  
16  
17  
18  
19 where  $m$  is the slope of the straight line in high field regime.  
20  
21

22  
23 Generally, the aspect ratio, screen effect and tip geometry of the nanostructures determine  
24 the  $\beta$ -value. By keeping the  $\varphi$  value as 5 eV,<sup>10,28</sup> the calculated  $\beta$  for the BNCD-CNS hybrids is  
25 6780. This value is greater than that of a carbon nanotube array (2916),<sup>9</sup> nitrogen doped diamond  
26 nanorods (3320),<sup>10</sup> graphene nanoflakes (1560),<sup>14</sup> graphene/carbon nanofilament (4930)<sup>20</sup> and  
27 diamond-like carbon-carbon nanotubes (5227).<sup>23</sup> The FEE lifetime ( $\tau_{FEE}$ -value) of the BNCD-  
28 CNS hybrids is a significant factor for field emission applications. To investigate the  $\tau_{FEE}$ -value  
29 of these BNCD-CNS hybrids, their emission was monitored for different applied voltages, 1.85  
30 V/ $\mu$ m, 1.90 V/ $\mu$ m, 1.95 V/ $\mu$ m and 1.98 V/ $\mu$ m above a period of 780 min, where the  $J_{FEE}$  value  
31 increases from 1.06 mA/cm<sup>2</sup>, 1.50 mA/cm<sup>2</sup>, 2.03 mA/cm<sup>2</sup> to 2.55 mA/cm<sup>2</sup>, respectively, with the  
32 increase of applied field (Figure 3b). In all cases, the fluctuations of the  $J_{FEE}$  are below 5% and  
33 the  $J_{FEE}$  values last for more than 780 min without showing signs of emission current decay,  
34 indicating excellent performance in emission stability for these hybrid materials. Interestingly,  
35 the FEE performance of the BNCD-CNS hybrids exhibits significant enhancements compared to  
36 other hybrid materials, as tabulated in Table S2.  
37  
38  
39  
40  
41  
42  
43  
44  
45  
46  
47  
48  
49  
50  
51  
52  
53  
54  
55  
56  
57  
58  
59  
60

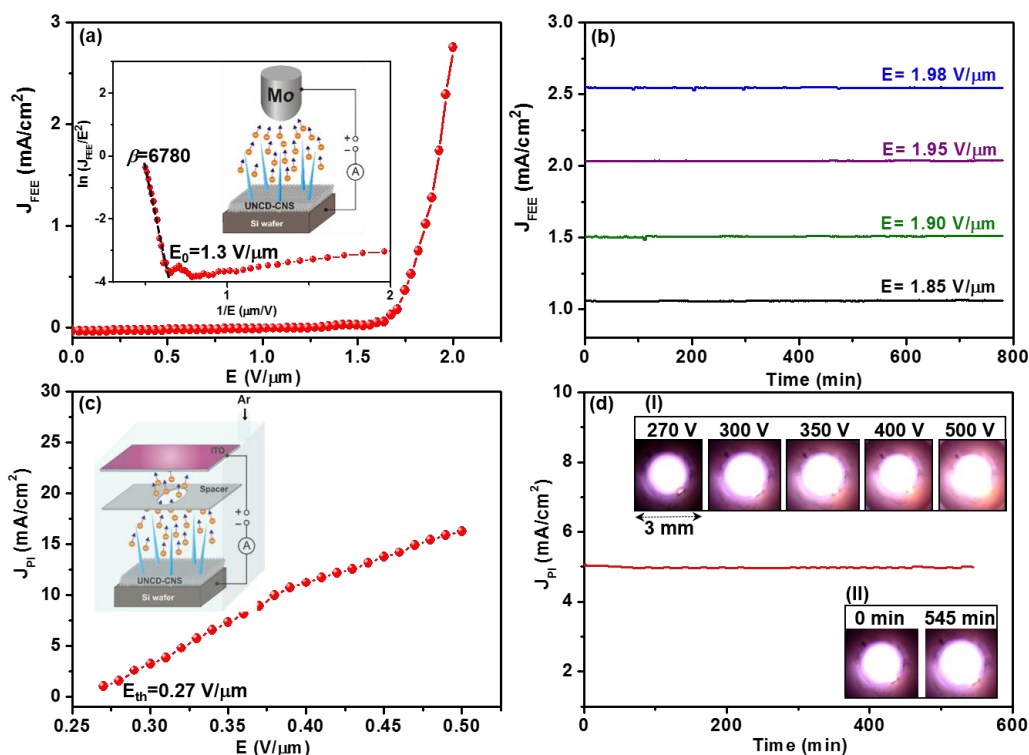


**Figure 3.** (a) Field electron emission (FEE) current density ( $J_{FEE}$ ) as a function of applied field ( $E$ ) for BNCD-CNS hybrids with the inset showing the F-N corresponding  $J_{FEE}-E$  characteristic curve along with the turn-on field ( $E_0=1.3$  V/ $\mu\text{m}$ ) and the schematic of the FEE measurement. (b) The lifetime stability test,  $J_{FEE}$  versus time curve, for hybrids at different applied fields. (c) The plasma current density ( $J_{PI}$ ) versus applied field ( $E$ ) of a microplasma cavity, which utilized ITO coated glass as anode and BNCD-CNS hybrids as cathode materials. The inset of (c) shows the schematic of the plasma illumination measurement set-up along with the threshold field ( $E_{th}=0.27$  V/ $\mu\text{m}$ ). (d) The plasma illumination stability of the BNCD-CNS hybrids. Inset I shows the photographs of the plasma illumination characteristics of the microplasma devices at varying voltages and inset "II" shows the plasma illumination intensity at 0 min and 545 min after ignition of the plasma, revealing that the plasma device essentially did not degrade even after long service time.

1  
2  
3 Furthermore, the localized FEE properties of the BNCD-CNSs hybrids were also  
4 investigated by AFM-based PF-TUNA technique<sup>40</sup> so as to directly locate the precise electron  
5 emission sites locally to understand the role of the BNCD and the CNSs materials on improving  
6 the FEE characteristics. Figure 4a shows the AFM surface morphology along with the  
7 representing PF-TUNA current mapping image (Figure 4b) of the BNCD films. The PF-TUNA  
8 current mapping was measured at an applied sample bias of -3.0 V. Figure 4a reveals that the  
9 BNCD films contain cauliflower-like aggregates of small diamond grains. The PF-TUNA image  
10 in Figure 4b reveals bright regions, which signify better electron emission. To locate exactly the  
11 field emission sites in the BNCD films, high resolution AFM (HRAFM) micrograph was taken  
12 (Figure 4c) with the corresponding PF-TUNA current mapping in Figure 4d. The bright and dark  
13 regions in the PF-TUNA image (Figure 4d) resembles the grain boundaries (GB) and grains (G)  
14 of the HRAFM image, which evidently illustrates that the electrons are predominantly emitted  
15 from the GBs (bright regions) rather than the grains (dark regions). Hence the more bright  
16 regions from the GBs prove that the existence of graphite at the GBs makes the electrons to  
17 transport very easily in the GBs. Moreover, a typical AFM micrograph of the whole BNCD-CNS  
18 hybrids is shown in Figure 4e and Figure 4f represents the PF-TUNA current mapping taken at a  
19 sample bias of -1.0 V corresponding to the AFM micrograph in Figure 4e. Again the brighter  
20 regions in Figure 4f signify more emission current. Consequently, it is evident through Figure 4f  
21 that the emission sites are preferentially seen from the CNSs and the darker regions are from the  
22 BNCD films because it is known that CNSs are more conductive than BNCD films.  
23  
24  
25  
26  
27  
28  
29  
30  
31  
32  
33  
34  
35  
36  
37  
38  
39  
40  
41  
42  
43  
44  
45  
46  
47  
48  
49  
50  
51  
52  
53  
54  
55  
56  
57  
58  
59  
60

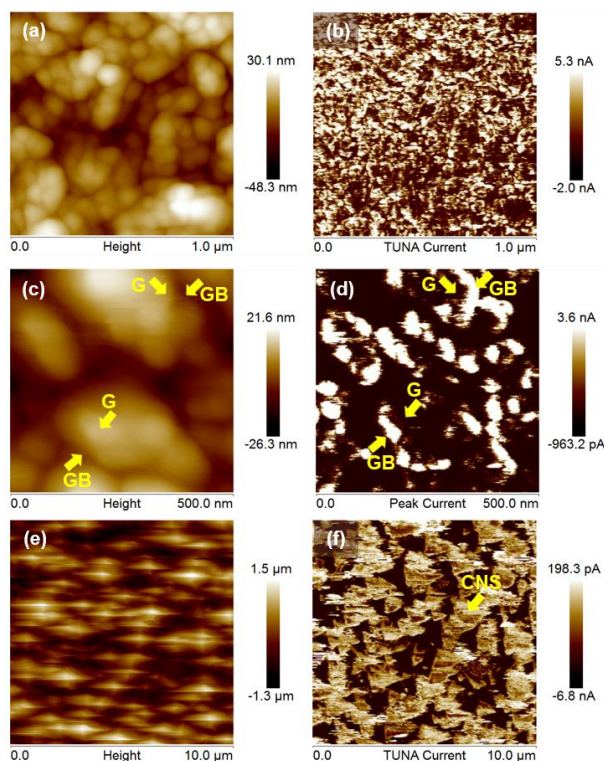


**Figure 4.** (a) AFM topography and (b) the corresponding PF-TUNA image corresponding to the BNCD region of the BNCD-CNS hybrids acquired at -3 V. (c) High resolution AFM and (d) the corresponding PF-TUNA image corresponding to the BNCD region of the BNCD-CNS hybrids acquired at -3 V. (e) AFM image of BNCD-CNS hybrids and (f) the corresponding PF-TUNA image acquired at -1 V.

The question to be answered is: What is the role of the boron and nitrogen, whose presence in the BNCD-CNS hybrids were confirmed through Raman, XPS and SIMS studies, on enhancing the FEE characteristics? First, in relation to boron doping, many debatable models have already been proposed for its behavior on enhancing the FEE properties. It is reported that the accumulation of holes due to boron doping increases the field enhancement,<sup>41</sup> besides the increase in the electrical conductivity of the BNCD films. A sub-band-based FEE model has also been proposed by other researchers.<sup>42</sup> Moreover, boron content in BNCD films is not reliable as

1  
2  
3 compared to the doping in microcrystalline diamond films.<sup>43</sup> Hence it is hard to draw a  
4  
5 conclusion on the effect of boron for enhancing the FEE of BNCD-CNS hybrids. Second, the  
6  
7 introduction of N<sub>2</sub> in diamond growth provides an amorphous phase. Upon annealing, the  
8  
9 amorphous phase at the grain boundaries was converted to a graphitic phase resulting in the  
10  
11 increase in the conduction paths for the electrons in the material. Therefore incorporation of N<sub>2</sub>  
12  
13 contributes to a rise in the density of states at the Fermi level, resulting in enhanced FEE  
14  
15 characteristics.<sup>44</sup> From the above observations, the superior FEE behavior of the BNCD-CNS  
16  
17 hybrids could be credited to the origin of sharp edges at the CNSs and the induction of the  
18  
19 graphitic phases at the grain boundaries of the BNCD films. The numerous vertically aligned  
20  
21 sharp geometric protrusions of the nanospikes with a smaller curvature radius facing the anode,  
22  
23 as shown in Figure 1a, which is commonly considered to have a fast electron transport rate, and  
24  
25 the sharp edges at the CNSs can enhance the local FEE,<sup>16,39</sup> thus resulting in the low  $E_0$  and high  
26  
27  $\beta$  values.  
28  
29  
30  
31  
32  
33

### 34 ***Microplasma source***

35  
36  
37 Microplasma sources are gas discharges in a small confined region that have recently received  
38  
39 huge interest owing to their numerous valuable characteristics, such as high electron density, low  
40  
41 power consumption, effectiveness with respect to cost, robustness and portability in  
42  
43 applications.<sup>45</sup> Principally, the devices based on microplasma sources create a novel area of  
44  
45 research connecting plasma science, materials science and optoelectronics.<sup>46</sup> Microplasma  
46  
47 devices are promising for several applications including microdisplays, hazardous gas detectors,  
48  
49 UV sources, plasma treatments, ozone production, silicon etching, and bioelectronics  
50  
51 applications.<sup>46-48</sup> Different kinds of materials such as Mo, Al<sub>2</sub>O<sub>3</sub>, boron nitride, zinc oxide,  
52  
53  
54  
55  
56  
57  
58  
59  
60

1  
2  
3 CNTs, and silicon have been applied as cathodes in microplasma devices.<sup>13,14,28,39,46</sup> But, these  
4 materials as the cathodes in the microplasma devices show short lifetimes and poor stability  
5 because the materials are exposed to a severe plasma ion bombardment.<sup>13,14,18,28,49</sup> Moreover, a  
6 cathode material for microplasma devices should possess a high proficiency in producing  
7 secondary electrons for a longer duration through plasma ion bombardment. The simulation  
8 work from Venkatraman *et al.* also show that a high FEE material can prominently improve the  
9 characteristics of a microplasma device.<sup>50</sup>  
10  
11  
12  
13  
14  
15  
16  
17  
18  
19

20 As BNCD-CNS hybrids possess superior FEE properties particularly in terms of high  
21 lifetime (cf. Figure 3b) and as particularly diamond has a high  $\gamma$ -coefficient, it is logical to apply  
22 BNCD-CNS hybrids as a microplasma device cathode. The plasma illumination (PI)  
23 characteristics of the BNCD-CNS hybrids-based cathode in a microplasma device carried out in  
24 a harsh Ar gas environment was shown in Figure 3c and Figure 3d. The corresponding  
25 measurement set-up for the microplasma device is shown in the inset of Figure 3c. The inset I of  
26 Figure 3d shows the PI images of the microplasma devices, which reveal that the plasma is  
27 triggered at a low voltage of 270 V and a systematic increase in the intensity of the plasma is  
28 observed while increasing the applied voltage. Figure 3c shows the plasma current density  
29 ( $J_{PI}$ )–applied field ( $E$ ) curve of the BNCD-CNS based microplasma devices. It can be seen that  
30 the plasma is ignited at a threshold field of  $E_{th}=0.27$  V/ $\mu$ m and the  $J_{PI}$  value reaches 16.2  
31 mA/cm<sup>2</sup> at  $E=0.50$  V/ $\mu$ m (applied voltage=550 V).  
32  
33  
34  
35  
36  
37  
38  
39  
40  
41  
42  
43  
44  
45  
46  
47  
48

49 Furthermore, the plasma lifetime stability ( $\tau_{PI}$ ) of BNCD-CNS hybrids was evaluated by  
50 monitoring the  $J_{PI}$  value of 5.0 mA/cm<sup>2</sup> (corresponding to  $E=0.32$  V/ $\mu$ m) over a long period of  
51 time. Figure 3d establishes that for the BNCD-CNS hybrids as microplasma cathodic devices,  
52  
53  
54  
55



1  
2  
3 the intensity of the plasma also remains stable after 545 min (inset II of Figure 3d), which  
4 indicates the high stability of these hybrids as compared to other diamond-based microplasma  
5 cathodic devices as reported (Table S3). Consequently, the benefit of the superior FEE properties  
6 as emitters, for the BNCD-CNS hybrids along with the high hardness and large  $\gamma$ -coefficient for  
7 the BNCD films, which reveals a high robustness and high plasma illumination intensity for  
8 these materials, shows that the BNCD-CNS hybrids have significant potential for application as a  
9 microplasma device cathode.  
10  
11  
12  
13  
14  
15  
16  
17  
18  
19

20 Now, the question yet to be answered is: Why do the BNCD-CNS hybrids, which possess  
21 a FEE turn-on field ( $E_0$ ) markedly larger than the plasma threshold field ( $E_{th}$ ), lead to enhanced  
22 PI performance? A potential description is as follows: before turning-on the Ar plasma, the  
23 BNCD-CNS hybrids employed as cathodes in the microplasma device required a threshold field  
24 ( $E_{th}$ ) to initiate the ignition of plasma. The  $E_{th}$  is low as compared to the FEE  $E_0$  value of the  
25 BNCD-CNS hybrids, and the secondary electrons only contribute for ionizing the Ar gas  
26 molecules. Hence, the relatively larger  $E_0$  of FEE is not helpful in contributing to the plasma  
27 current density ( $J_{PI}$ ) of the microplasma devices. But once the plasma is triggered, a few micron  
28 thick plasma sheath is generated near to the cathode. The bulk of the plasma performed as an  
29 electron conduction path so that the voltage supplied to the anode will apply onto the plasma  
30 sheath. The electric field applied to the cathode will increase to around 0.32 V/ $\mu\text{m}$  (e.g. for an  
31 applied voltage of 320 V with 10  $\mu\text{m}$  plasma sheath), which is noticeably higher than the FEE  $E_0$   
32 value ( $E_0=1.3$  V/ $\mu\text{m}$ ). The BNCD-CNS hybrids emit enormous numbers of electrons and the  
33 plasma is ignited once the emitted electrons from the material attain the large kinetic energy of  
34 15.7 eV adequate for ionizing the Ar gas molecules, and consecutively, there is an increase in the  
35  
36  
37  
38  
39  
40  
41  
42  
43  
44  
45  
46  
47  
48  
49  
50  
51  
52  
53  
54  
55  
56  
57  
58  
59  
60

1  
2  
3 ionization of the Ar gas molecules along with a noticeable increase in the plasma density.  
4  
5 Consequently, BNCD-CNS hybrids achieved a higher  $J_{PI}$ -value when employing them as  
6  
7 cathodes in a microplasma device.  
8  
9

## 10 **TEM Microstructure**

11  
12  
13  
14 To understand why the BNCD-CNS hybrids exhibit superior FEE and microplasma behaviors,  
15  
16 the microstructure and the bonding structure of these hybrids were investigated by transmission  
17  
18 electron microscopic (TEM) and electron energy loss spectroscopy (EELS). A low-magnification  
19  
20 bright field TEM micrograph (BF-TEM) for the BNCD films is displayed in inset “a<sub>1</sub>” of Figure  
21  
22 5a, suggesting the formation of carbon nanoclusters of acicular geometry evenly distributed  
23  
24 among the amorphous carbon matrix. Figure 5a shows a high-magnified TEM micrograph of the  
25  
26 marked area “A” from inset “a<sub>1</sub>” in Figure 5a, which evidently shows the existence of acicular  
27  
28 nanoclusters (dark contrast). The selective area electron diffraction (SAED) pattern (inset “a<sub>2</sub>” of  
29  
30 Figure 5a), corresponding to the high-magnified TEM micrograph, contains diffraction rings  
31  
32 representing the (111), (220), and (311) diamond lattices and the presence of  $sp^2$ -bonded carbon  
33  
34 in this hybrid is indicated by a very bright diffuse ring at the center of the SAED pattern. Dark-  
35  
36 field (DF) images are used to clearly elucidate the distribution of the phase constituents in the  
37  
38 material, which were acquired from the diffraction segments of the SAED corresponding to the  
39  
40 diamond and graphite phases (yellow and green rings; inset “a<sub>2</sub>” of Figure 5a) and then  
41  
42 superimposed to form a composed dark field (c-DF) image. The c-DF image displayed in Figure  
43  
44 5b noticeably reveals the presence of acicular nanoclusters, which are of graphitic phases (green  
45  
46 color), and the nanosized diamond grains (yellow color). These phases were distributed evenly  
47  
48 among the matrix, which are amorphous carbon, in the BNCD region.  
49  
50  
51  
52  
53  
54  
55

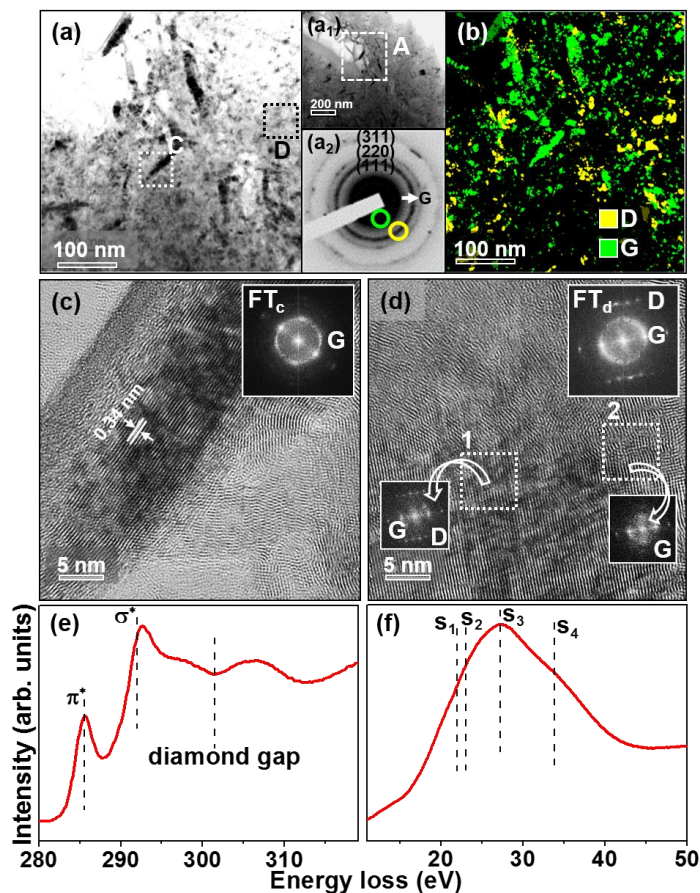


**Figure 5.** (a) A high magnification bright field TEM (BF-TEM) micrograph corresponding to the BNCD region of the BNCD-CNS hybrids. Image “a” is taken from region “A” designated in the low magnification BF-TEM image, which is shown as inset “a<sub>1</sub>”, whereas the corresponding SAED pattern is shown as inset “a<sub>2</sub>”. (b) The composed dark field TEM image corresponding to the TEM micrograph in “a” to mark the diamond and graphite regimes. (c) High resolution TEM micrograph, the structure image, taken at the region marked as “C” in “a” with the Fourier transformed diffractogram corresponding to entire structure image is shown as the inset. (d) High resolution TEM micrograph, the structure image, taken at the region marked as “D” in “a” with the Fourier transformed diffractogram corresponding to entire structure image shown as inset “FT<sub>d</sub>” whereas the regions “1” and “2” show the FT images corresponding to diamond and

1  
2  
3 graphite phases, respectively. (e) Core-loss and (f) plasmon-loss EELS spectra of the BNCD-  
4  
5 CNS hybrids corresponding to BF-TEM micrograph in “a.”  
6  
7

8  
9 Figure 5c and 5d show the HRTEM micrographs of the BNCD films corresponding to the  
10 regions “C” and “D” in Figure 5a. The Fourier transformed (FT) diffractogram of the whole  
11 structure image in Figure 5c,  $FT_c$ , illustrates the diffraction spots organized in a ring representing  
12 the graphitic phase. Moreover, the 0.34 nm interlayer spaced parallel fringes in the inset of  
13 Figure 5c confirm that the acicular nanoclusters are only crystalline nanographite.<sup>51</sup> But Figure  
14  
15 5d contains both nanosized diamond particulates and graphitic phases, which are identified from  
16 the  $FT_d$  image, corresponds to the whole structure image of Figure 5d, containing faint  
17 diffraction spots indicating diamond (designated as D) and a strong new-moon-like central  
18 diffused ring indicating graphite (designated as G), respectively. The FT images shown as the  
19 inset of Figure 5d, which correspond to the regions marked “1 and 2” in Figure 5d, indicate the  
20 diamond and graphitic phases, respectively.  
21  
22  
23  
24  
25  
26  
27  
28  
29  
30  
31  
32  
33

34  
35 The carbon K-edge EELS in TEM was used to study the different carbon phases in the  
36 BNCD films. The core-loss EELS spectrum of the BNCD films shown in Figure 5e indicates that  
37 the BNCD films contain both  $sp^3$ -bonded carbon (i.e. diamond), represented by a sharp peak at  
38 291 eV ( $\sigma^*$ -band) and a dip in the vicinity of 302 eV,<sup>52</sup> and  $sp^2$ -bonded carbon specified by a  $\pi^*$ -  
39 band at 285 eV.<sup>53</sup> The plasmon-loss EELS measurements in TEM were further carried out to  
40 discriminate between graphite and amorphous carbon phases. Figure 5f shows the plasmon-loss  
41 EELS spectrum of the BNCD films, which reveals a peak around 27 eV ( $S_3$ ) confirms the  
42 presence of graphite and a peak near 33 eV ( $S_4$ ) along with a shoulder near 23 eV ( $S_2$ ) (Figure  
43 5f) indicate the presence of diamond in the BNCD films.<sup>54</sup> The peak at 22 eV ( $S_1$ ) representing  
44  
45  
46  
47  
48  
49  
50  
51  
52  
53  
54  
55

amorphous carbon phase is not evident in Figure 5f. Based on these TEM and EELS investigations in Figure 5, it is evident that the BNCD materials contain a mixture of nanosized diamond grains of equi-axed geometry and well crystallized nanographitic clusters of acicular geometry, along with a large proportion of randomly oriented spherical nanographitic clusters, distributed among the amorphous carbon matrix.

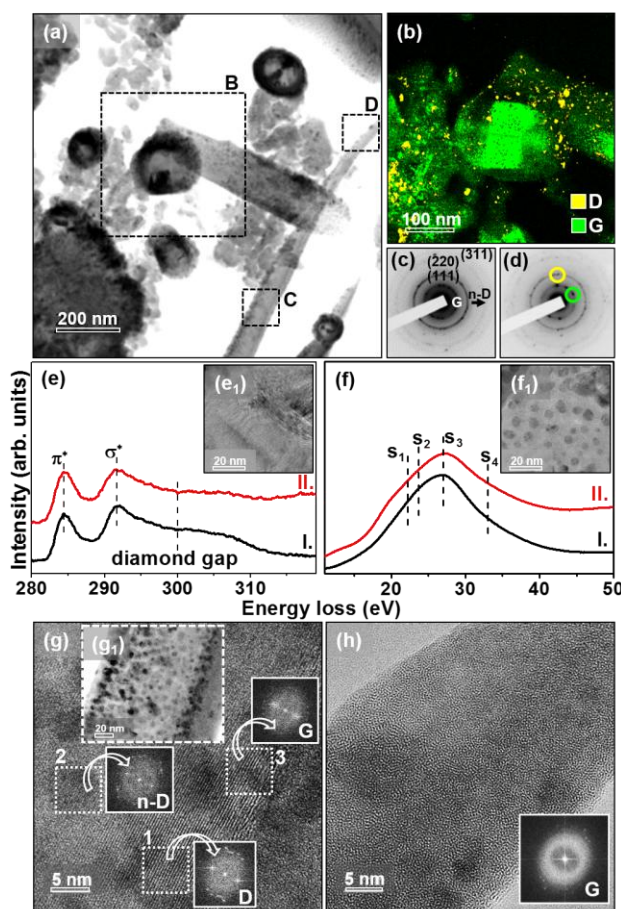


**Figure 6.** (a) A bright field TEM (BF-TEM) micrograph corresponding to the spike region of the BNCD-CNS hybrids whereas the corresponding SAED pattern is shown “c”. (b) The composed dark field (DF) TEM image corresponding to region “B” of “a”. The DF images were acquired from different segments of SAED shown in “d” and then superimposed, where the D region (yellow color) are diamond and G region (green color) are graphitic phase. Spectra “I” in “e” and

1  
2  
3 “f” represent the core-loss and plasmon-loss carbon K-edge EELS spectrum of spherical balls  
4 (region B in “G”), whereas spectrum II in “e” and “f” represent the core-loss and plasmon-loss  
5 carbon K-edge EELS spectrum taken from the structure image at the bottom region of the  
6 nanospikes (“D” region in “a”). (g) The high resolution TEM micrograph, the structure image, of  
7 the region shown as the bright field TEM micrograph in inset  $g_1$ , which was taken from region C  
8 of “a”, representing the bottom region of the nanospike. The regions “1”, “2” and “3” show the  
9 FT images corresponding to diamond, *n-D* and graphite phases, respectively. (h) The structure  
10 image taken from region D of “a”, which represents that the top region of the nanospikes are  
11 only graphitic in nature. This is understood from the FT image (inset of “h”) that corresponds to  
12 the whole structure image in “h”.  
13  
14  
15  
16  
17  
18  
19  
20  
21  
22  
23  
24  
25  
26

27 Figure 6 shows the TEM microstructure of CNSs. The BF-TEM micrograph of the CNSs  
28 displayed in Figure 6a discloses the existence of ball-like nanostructures of size around 50–200  
29 nm as well as the needle-like CNSs that are about 100–200 nm in width. The SAED pattern  
30 shown as Figure 6c corresponding to the BF-TEM of Figure 6a brings out the presence of the  
31 (111), (220), and (311) diffraction rings, along with the existence of a strong central diffused  
32 ring, revealing that the CNSs are predominately the  $sp^2$ -bonded graphitic phase. Remarkably, a  
33 ring shaped extra weak diffraction spots specified by an arrow in the inset of Figure 6c agrees to  
34 an allotrope of diamond called (200) *n-diamond* (*n-D*) with a cell parameter of 0.356 nm and a  
35 space group of Fm3m symmetry).<sup>52,55</sup> The *n-D* clusters can be viewed as incompletely  
36 crystallized diamond clusters, that is, they formed earlier than the development of diamond  
37 nuclei. The magnified c-DF image in Figure 6b taken from region ‘B’ of Figure 6a, which was  
38 acquired from different segments of SAED shown in Figure 6d, clearly shows that the spherical  
39  
40  
41  
42  
43  
44  
45  
46  
47  
48  
49  
50  
51  
52  
53  
54  
55  
56  
57  
58  
59  
60

1  
2  
3 balls are of graphitic phases (green color) and the nanosized diamond particulates (yellow color)  
4  
5 are evenly distributed surrounding the spherical graphitic balls. The carbon K-edge core-loss  
6  
7 EELS spectrum I taken from the structure image of spherical balls (inset I of Figure 6e) indicates  
8  
9 the  $\pi^*$  band at 285.0 eV, representing these spherical balls are comprised of only graphitic  
10  
11 phases and no diamond phase. The plasmon-loss EELS spectrum I in Figure 6f confirms the  
12  
13 findings from the core-loss EELS spectrum I in Figure 6f.  
14  
15  
16  
17

18 The high-magnified TEM micrograph shown in inset  $g_1$  of Figure 6g, which was taken  
19  
20 from region C of Figure 6a, indicates that the bottom region of the nanospikes contains  
21  
22 nanosized clusters around 5–10 nm in size. The structure image displayed in Figure 6g clearly  
23  
24 specifies that this bottom region contains different phases; nanosized diamond (FT<sub>1</sub>), *n-D* (FT<sub>2</sub>)  
25  
26 and graphite (FT<sub>3</sub>) phases. The core-loss (spectrum II of Figure 6e) and plasmon-loss spectra  
27  
28 (spectrum II of Figure 6f) (cf. HRTEM micrograph of Figure 6g) further confirm that this bottom  
29  
30 region is predominated with graphitic nanoclusters. It is to be noted that signature of diamond  
31  
32 peaks from core-loss EELS (spectrum II, Figure 6e) is absent, demonstrating that the diamond  
33  
34 lattices contain more defects such as *n-D* particulates. In contrast, the top region of the  
35  
36 nanospikes are only graphitic in nature, which is understood from the structure image in Figure  
37  
38 6h taken from region D of Figure 6a and the FT image (inset of Figure 6h) that relates to the  
39  
40 whole HRTEM micrograph in Figure 6h. Consequently, combining the description of the  
41  
42 microstructure of BNCD-CNS hybrids implies that these materials are actually nanocarbon  
43  
44 hybrid materials, which are predominantly with well crystallized graphitic clusters dispersed  
45  
46 with the nanosized diamond particulates.  
47  
48  
49  
50  
51  
52

### 53 **Formation mechanism**

54  
55  
56  
57  
58  
59  
60

1  
2  
3 It should be noted that the TEM microstructures and the EELS spectra shown in Figure 5 and  
4 Figure 6 clearly indicate that the nanodiamond clusters contained in the materials gradually  
5 disappeared while the CNSs grew. This implies that CNSs probably stemmed from the acicular  
6 nanographite clusters enclosed in the BNCD layer, which are predominantly the graphite phase.  
7  
8 In order to examine the growth mechanism of the BNCD-CNS hybrids, together with the  
9 identification of carbon allotropes in the BNCD-CNS hybrids, the optical emission spectroscopy  
10 (OES) spectra of microwave plasma during the biased carburization (phase I) and growth (phase  
11 II) stages were recorded. Figure 7 shows that the emission spectra of the plasma recorded during  
12 two different phases of the CVD process do not show substantial differences. This observation  
13 implies that the difference in formation process of BNCD and CNS is mainly driven by the  
14 reactions of the growth plasma and surface induced by the biased voltage. The important species  
15 contained in the OES spectra are listed in Table S4. The growth process of BNCD-CNS hybrids  
16 involves H, a  $\text{CH}_x$  band at 431.4 nm, a  $\text{N}_2$  band at 358 nm, a CN band at 418 nm, and  $\text{C}_2$  Swan  
17 bands at 516.5 nm,<sup>56</sup> respectively, which show a major part in the origin of the diamond and  
18 graphitic phases. The ratios of intensity of the  $\text{C}_2$  band at 516.5 nm associated to the  $\text{H}_\beta$  lines  
19 ( $\text{C}_2/\text{H}_\beta$ ) reach values up to 0.66 and 0.78 for the biased enhanced carburization (spectrum I) and  
20 standard CVD growth phases (spectrum II), respectively. The  $\text{C}_2$  species are the cause for the  
21 formation of single carbon species that shape the structure or nucleate the spikes. Furthermore,  
22 the CH relative to  $\text{H}_\beta$  line ( $\text{CH}/\text{H}_\beta$ ) reveals a decrease in the value from 1.56 to 1.47 for biased  
23 enhanced carburization (phase I) and standard CVD growth (phases II) stages, respectively. The  
24 surface of the diamond seeds and clusters are attached by the CN and HCN species, which  
25 enriches the diamond growth, whereas the presence of CH species tends to passivate the as-  
26 formed diamond nuclei, preventing the diamond nuclei to grow further as a large sized diamond  
27  
28  
29  
30  
31  
32  
33  
34  
35  
36  
37  
38  
39  
40  
41  
42  
43  
44  
45  
46  
47  
48  
49  
50  
51  
52  
53  
54  
55



grain, which explains why the diamond particles in BNCD films remained very small size. Furthermore, the BH band at 433 nm showed in Figure 7 represents the fingerprint of boron in the growth plasma, confirming the BNCD bottom layer and CNSs are doped with boron. The BH emission is slightly larger during phase biased enhanced carburization (phase I) than standard CVD growth phases (phase II).

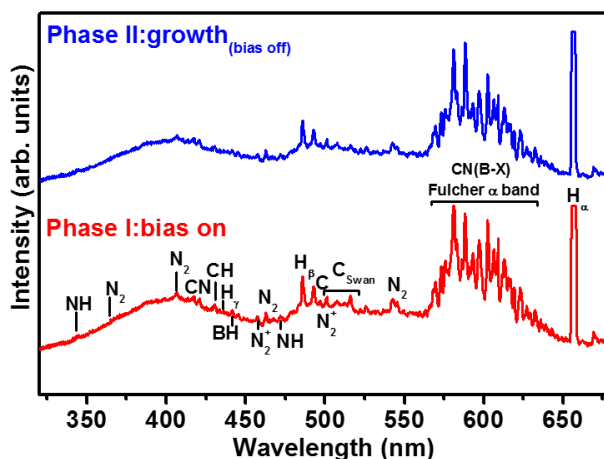


**Figure 7.** The OES spectra of the  $\text{H}_2/\text{CH}_4/\text{B}_2\text{H}_6/\text{N}_2$  microwave plasma during biased carburization (phase I) and growth (phase II). The emission spectra recorded during these two different CVD phases do not show substantial variances. The growth process of BNCD-CNS in the presence of nitrogen involves H,  $\text{CH}_x$ , and CN radicals. The presence of an  $\text{N}_2$  band at 358 nm, and a CN band at 418 nm confirms the contribution of nitrogen-based species in the plasma. These nitrogen species modify the plasma reactions by changing the concentrations of other growth species such as  $\text{C}_2$  and CH ( $\text{C}_2$  Swan bands at 516.5 nm; CH line at 431.4 nm), and play a key role in the formation of diamond and graphitic phases. The plasma chemistry of the boron precursor, i.e. diborane ( $\text{B}_2\text{H}_6$ ), is evidenced by the BH band at 433 nm, the most representative fingerprint of boron in the plasma.

1  
2  
3 Nevertheless, the change in abundance of the  $C_2$ ,  $N_2$ ,  $H_x$ ,  $CH_x$ ,  $CN$ ,  $BH$  radicals attributable  
4 to the bias applied in phase I (bias-enhanced carburization) is not significant and seems not to be  
5 the main feature resulting in the change of the growth mechanism to form the BNCD and CNSs.  
6 On the other hand, the kinetic energy of the charged carbonaceous species increases noticeably  
7 due to the application of bias. It has been observed recently that the rise in kinetic energy of the  
8 adsorbed species, no matter whether it results from the increase in substrate temperature or the  
9 application of bias voltage, facilitates the crystallization of the adsorbed adatoms.<sup>57</sup> Among the  
10 important species exist in the  $CH_4/H_2/B_2H_6/N_2$  plasma, the  $C_2$  and  $CH$  species grow  
11 carbonaceous materials (diamond, graphite and amorphous carbons), whereas the  $CN_x$  and  $H_x$  etc  
12 are the species which modify the microstructure of the phases. The formation of crystalline  
13 clusters is difficult at the present of complicated species in the  $CH_4/H_2/B_2H_6/N_2$  plasma,  
14 especially in the presence of  $CH_x$  and  $CN_x$  species. Therefore, the phase II (growth phase) tends  
15 to grow amorphous carbons or related materials. Only when the bias is applied can the adsorbed  
16  $C_2$  species form crystalline clusters. In the bias enhanced carburization phase (phase I), the  
17 nanographitic clusters will form preferentially, as they were energetically favorable, as compared  
18 with the formation of nanodiamond clusters.<sup>49,57,58</sup> Moreover, the nanographitic clusters are of  
19 acicular geometry which is also attributable to the application of this bias. This process explains  
20 excellently the growth of the BNCD layer in phase I. When no bias is applied in the growth  
21 period (phase II), the matrix of amorphous carbon ceases to grow. Only the acicular nanographitic  
22 clusters serve as the nuclei for the growth of nanospikes.  
23  
24  
25  
26  
27  
28  
29  
30  
31  
32  
33  
34  
35  
36  
37  
38  
39  
40  
41  
42  
43  
44  
45  
46  
47  
48  
49

50 The above described processes for the formation of the BNCD bottom layer and  
51 subsequently the outgrowth of the spike-like carbon nanostructures is schematically illustrated in  
52 Figure 8. That is, because of the application of bias, the carbon clusters start to form nanosized  
53  
54  
55

1  
2  
3 crystalline clusters ( $sp^2$ - or  $sp^3$ -bonded carbons) as well as amorphous carbon as a matrix (Figure  
4 8b). Notably, the pre-seeding procedure (Figure 8a) is necessary to induce the nucleation of  
5 nanosized crystalline clusters. During the phase I process, some nanographitic clusters of  
6 acicular geometry were induced. The nanodiamond particulates of equi-axed geometry were also  
7 formed occasionally, evenly distributed among the amorphous carbon matrix that resulted in  
8 BNCD layers. In phase II of the MWPECVD process, the bias voltage was removed. The growth  
9 of the BNCD layer ceased owing to the insufficient kinetic energy of the species. Only the  
10 nanographitic clusters continued to grow due to the smaller surface energy for the formation of  
11 graphite materials and the existence of nanographitic nanoneedles, which serve as nanospike  
12 nuclei. The scheme shown in Figure 8 is in agreement with other previous findings<sup>58,59</sup> and  
13 supported by the SEM, Raman, XPS and TEM studies reported in this paper.  
14  
15  
16  
17  
18  
19  
20  
21  
22  
23  
24  
25  
26  
27  
28



42 **Figure 8.** Scheme of the growth mechanism of BNCD-CNS hybrids in the  $H_2/CH_4/B_2H_6/N_2$   
43 microwave plasma-(a) the nanodiamond seeding on the Si wafer prior to diamond growth, (b)  
44 and (c) the sub-sequential steps of nanospike formation of BNCD-CNS hybrids in the microwave  
45 plasma.  
46  
47  
48  
49

## 50 ■ CONCLUSIONS

1  
2  
3 This work presents a one-step fabrication of hybrid carbon materials based on CNS together with  
4 a BNCD layer. This hybrid structure overwhelms numerous problems that of in the CNT tips,  
5 especially in a plasma environment. The synthesized BNCD-CNS hybrids showed superior FEE  
6 properties with a low  $E_0$  of 1.3 V/ $\mu\text{m}$ , a large  $\beta$ -factor of 6780, a high  $J_{\text{FEE}}$  of 2.7 mA/cm and a  
7 long-lasting electron emission stability of 780 min at different applied fields. The excellent FEE  
8 properties of these hybrids are derived mainly from the synergistic effects between CNS and  
9 BNCD, which possess large aspect ratio and numerous emission sites. Such hybrids not only  
10 exhibit excellent FEE properties then also display high robustness in a plasma environment when  
11 they are employed as a cathode in a microplasma device. Overall, this study proposes that the  
12 presented BNCD-CNS hybrids appear as a prospective electron source for flat panel displays and  
13 plasma displays.  
14  
15  
16  
17  
18  
19  
20  
21  
22  
23  
24  
25  
26  
27

## 28 ■ EXPERIMENTAL METHODS

29  
30  
31 *Catalyst free, one-step growth of BNCD-CNS:* A MWPECVD (2.45 GHz SEKI  
32 Technotron AX5400S, Japan) system was used to synthesize the BNCD-CNS hybrids on silicon  
33 substrates. Prior to the CVD growth, Si substrates were nucleated in diamond slurry (BlueSeeds,  
34 AdamasNano, USA) by ultrasonication process. It is reported that a high seeding density of  $10^{10}$   
35  $\text{cm}^{-2}$  was achieved using this seeding procedure.<sup>60</sup> Studied surfaces have been grown utilizing  
36 the following growth parameters: gas mixture —  $\text{H}_2 : \text{CH}_4 : \text{B}_2\text{H}_6 : \text{N}_2$  (85:5:9:1%) of total flow  
37 rate 265 sccm; [B]/[C] ratio of (0.0167%) 16700 ppm; microwave power set to 1100 Watts;  
38 process pressure of 35 Torr; and a growth time equal to 20 hours. An induction heater was  
39 employed to heat the substrate holder to 650°C and a thermocouple was used to measure the  
40 substrate temperature. To enhance the seeding and nucleation process of the BNCD-CNS  
41  
42  
43  
44  
45  
46  
47  
48  
49  
50  
51  
52  
53  
54  
55  
56  
57  
58  
59  
60

1  
2  
3 surfaces, a negative bias voltage of -200 V was applied to the stage during the first 20 minutes of  
4  
5 CVD growth.  
6

7  
8 ***Material Characterization:*** The surface morphology, the microstructure and the bonding  
9  
10 structure of these hybrid materials were examined with a scanning electron microscope (SEM;  
11  
12 FEI Quanta FEG 250 using a 10 kV beam accelerating voltage with an SE-ETD (secondary  
13  
14 electron Everhart–Thornley detector) working in high-vacuum mode (pressure  $10^{-4}$  Pa)), a  
15  
16 transmission electron microscopy (TEM, Jeol 2100F) and an electron energy loss spectroscopy  
17  
18 (EELS, Gatan Enfina) in the TEM, respectively. The Raman spectra of the materials were  
19  
20 recorded using a micro Raman spectrometer (InVia, Renishaw, UK) equipped with a 514 nm  
21  
22 argon-ion laser as an excitation source in combination with a  $50\times$  objective (NA = 0.5) and a 10  
23  
24  $\mu\text{m}$  confocal aperture. Spectra were recorded in a range of  $100\text{--}3200\text{ cm}^{-1}$ . High-resolution X-ray  
25  
26 photoelectron spectroscopy (XPS) studies were carried out on an Escalab 250 Xi from  
27  
28 Thermofisher Scientific. The spectroscope is equipped with Al  $K\alpha$  source. The pass energy was  
29  
30 20 eV and the spot size diameter was  $650\text{ }\mu\text{m}$ . Charge compensation was controlled through the  
31  
32 low-energy electron and low energy  $\text{Ar}^+$  ions emission by means of a flood gun (emission  
33  
34 current  $150\text{ }\mu\text{A}$ , beam voltage 2.1 V, filament current 3.5 A). Avantage software (Thermofisher  
35  
36 Scientific) was used for deconvolution purposes. Elemental depth profiling analysis of the C, B,  
37  
38 BN, CN and N in BNCD-CNS samples was carried out by time of flight SIMS (TOF-SIMS5,  
39  
40 ION-TOF GmbH) using Bismuth ( $\text{Bi}^+$ ) ion. Two-dimensional (2D) images of the depth profiling  
41  
42 were generated for the quantitative elemental analysis. The plasma constituents were analyzed by  
43  
44 OES using a 0.3 m monochromator (SR303i, Andor) equipped with a 1200 grooves per mm  
45  
46 grating and ICCD detector (DH740, Andor).  
47  
48  
49  
50  
51  
52  
53  
54  
55  
56

1  
2  
3       ***FEE Measurements:*** To evaluate the FEE performance of the BNCD-CNS hybrids, a  
4 hybrid was installed in a high vacuum chamber of pressure below  $10^{-6}$  Torr. A custom-made  
5 tunable parallel plate capacitor, with a molybdenum tip of 2 mm diameter, was used as the anode  
6 at a fixed distance of 200  $\mu\text{m}$  from the cathode (emitting sample). The separation of the anode  
7 from the sample was measured using a digital micrometer. The setup was completed by  
8 electrically connecting the electrodes to a computer-controlled Keithley K2410 source/measure  
9 unit to acquire the current densities versus electrical field ( $J_e$ - $E$ ) characteristics and the data were  
10 analyzed using F-N theory.  
11  
12  
13  
14  
15  
16  
17  
18  
19  
20

21       ***PF-TUNA Measurements:*** A multi-mode VIII AFM with a Nanoscope V controller  
22 and PF-TUNA module [Bruker, CA, USA] were used to perform the PF-TUNA measurements  
23 at ambient conditions. The measurement details have been elucidated elsewhere.<sup>60</sup> In brief, to  
24 create electrical contact between the BNCD-CNS hybrids and the AFM tip, conductive silver  
25 paint (G3790 Agar Scientific) was used to attach the base of the Si substrate to a metallic disc.  
26 PeakForce feedback helped to collect the topographic and tunneling current information. A Pt-Ir  
27 coating on the tip of the cantilever, with a spring constant of 9.8 N/m, allowed the measurement  
28 of current from the sample surface when a bias was applied between the tip and the sample.  
29 Images were recorded at a resolution of  $512 \times 512$  pixels with a tip bias of a few volts with a  
30 lower scan rate of 0.1 or 0.2 Hz to allow the maximum time for the TUNA current measurement  
31 in a particular position. A number of tests were performed to confirm that the measured TUNA  
32 current is a true reflection of the emission current of the BNCD-CNS surface and not from any  
33 artifacts present on the surface. The recorded emission currents, with tip-sample biases varying  
34 from the mV to V range, were in the range of few pA to a few nA per emission site.  
35  
36  
37  
38  
39  
40  
41  
42  
43  
44  
45  
46  
47  
48  
49  
50  
51  
52  
53  
54  
55  
56  
57  
58  
59  
60

**PI Measurements:** The PI characteristics of the BNCD-CNS hybrids were evaluated using a microplasma device with parallel plate configuration, in which the indium-tin oxide (ITO) coated glass plates (the anode) were separated from the cathode (BNCD-CNS hybrids) by a 1.0 mm thick Teflon<sup>TM</sup> spacer. A 3.0 mm in diameter circular hole was cut out of the Teflon spacer to create a cylindrical cavity. The devices were kept in a vacuum chamber with a base pressure of 0.01 mTorr and externally connected to a DC power supply through a 500 k $\Omega$  resistor. The reliability of the measurements were improved by heating the samples at 200 °C for 1 h to remove any moisture on the surface of the samples. Argon at the rate of 10 sccm was flowed throughout the measurements and a plasma was excited in between the ITO and BNCD-CNS hybrids by supplying a DC voltage from 0 V to breakdown and then was increased linearly up to the maximum voltage of 500 V (at room temperature). The plasma current density ( $J_{PI}$ ) versus applied field (E) was acquired at a constant pressure of 100 Torr using a Keithley 2410 current source electrometer. The plasma was observed through the ITO using a USB microscope and snapshots were recorded for different applied voltages to characterize the PI behavior of the microplasma devices.

## ■ ASSOCIATED CONTENT

### Supporting Information

The Supporting Information is available free of charge on the ACS Publications website at DOI: Two-dimensional mapping of SIMS depth profiles of the growth species such as C<sub>2</sub>, BH, CH, CN, and B in the H<sub>2</sub>/CH<sub>4</sub>/B<sub>2</sub>H<sub>6</sub>/N<sub>2</sub> plasma. The C<sub>2</sub> species possess high intensity with high bright regions. The BH and CH species are almost at the same intensity followed by the CN, O and B species (Figure S1). High-resolution XPS analysis of different *C1s*, *B1s* and *N1s* chemical states in the BNCD-CNS hybrids, deconvoluted using the above-described model (Table S1). Field

1  
2  
3 electron emission properties of BNCD-CNS hybrids compared to other hybrid nanostructures  
4 reported in literature (Table S2). Plasma illumination properties of BNCD-CNS hybrids  
5 compared to other diamond based microplasma cathodic devices reported in literature (Table S3).  
6  
7  
8 The designation of the species derived from the OES spectra of the CH<sub>4</sub>/H<sub>2</sub>/B<sub>2</sub>H<sub>6</sub>/N<sub>2</sub> plasma used  
9  
10 for growing the BNCD and CNSs (Table S4).  
11  
12  
13  
14  
15  
16

## 17 ■ AUTHOR INFORMATION

18  
19 Corresponding Authors

20  
21 \*E-mail: sankaran.kamatchi@uhasselt.be

22  
23 \*E-mail: ken.haenen@uhasselt.be

24  
25  
26 Notes

27  
28 The authors declare no competing financial interest.  
29  
30  
31  
32

## 33 ■ ACKNOWLEDGEMENTS

34  
35 This work is supported by the Flemish Methusalem “NANO” network, the Polish National  
36 Science Centre (NCN) under Grant Nos. 2014/14/M/ST5/00715, 2015/17/D/ST5/02571 and  
37 2016/21/B/ST7/01430, and the Institute for Basic Science [IBS-R004]. The DS funds of the  
38 Faculty of Electronics, Telecommunications and Informatics of the Gdansk University of  
39 Technology are also acknowledged. The manuscript was written through contributions of all  
40 authors. All authors gave approval to the final version of the manuscript. K. J. Sankaran and M.  
41 Ficek contributed equally to this work.  
42  
43  
44  
45  
46  
47  
48  
49  
50  
51  
52  
53

## 54 ■ REFERENCES



1  
2  
3 (1) Fowler, R. H.; Nordheim, L.; Electron Emission in Intense Electric Fields. *Proc. R. Soc.*  
4  
5 *London, Ser. A.* **1928**, *119*, 173–181.

6  
7  
8 (2) Xavier, S.; Tempfli, S. M.; Ferain, E.; Purcell, S.; Vedrenne, S. E.; Gangloff, L.; Minoux,  
9  
10 E.; Hudanski, L.; Vincent, P.; Schnell, J. P.; Pribat, D.; Piraux, L.; Legagneux, P. Stable Field  
11  
12 Emission from Arrays of Vertically Aligned Free-standing Metallic Nanowires. *Nanotechnology*  
13  
14 **2008**, *19*, 215601.

15  
16  
17 (3) Collins, C. M.; Parmee, R. J.; Milne, W. I.; Cole, M. T. High Performance Field Emitters.  
18  
19 *Adv. Sci.* **2016**, *3*, 1500318.

20  
21 (4) Zhang, Q. Y.; Xu, J. Q.; Zhao, Y. M.; Ji, X. H.; Lau, S. P. Fabrication of Large-Scale  
22  
23 Single-Crystalline PrB6 Nanorods and Their Temperature-Dependent Electron Field Emission.  
24  
25 *Adv. Funct. Mater.* **2009**, *19*, 742–747.

26  
27 (5) Viskadourous, G.; Zak, A.; Stylianakis, M.; Kymakis, E.; Tenne, R.; Stratakis, E. Enhanced  
28  
29 Field Emission of WS<sub>2</sub> Nanotubes. *Small* **2014**, *10*, 2398–2403.

30  
31 (6) Pradhan, D.; Kumar, M.; Ando, Y.; Leung, K. T. Efficient Field Emission from Vertically  
32  
33 Grown Planar ZnO Nanowalls on an ITO-Glass Substrate. *Nanotechnology* **2008**, *19*, 035603.

34  
35 (7) Chen, L.; Yu, H.; Zhong, J.; Wu, J.; Su, W. Graphene based Hybrid/Composite for  
36  
37 Electron Field Emission: A Review. *J. Alloy Compd.* **2018**, *749*, 60–84.

38  
39 (8) Xu, J.; Chang, Y.; Gan, L.; Ma, Y.; Zhai, T. Ultrathin Single-Crystalline Boron  
40  
41 Nanosheets for Enhanced Electro-Optical Performances. *Adv. Sci.* **2015**, *2*, 1500023.

1  
2  
3 (9) Zhang, Q.; Wang, X.; Meng, P.; Yue, H.; Zheng, R.; Wu, X.; Cheng, G. High Current  
4 Density and Low Emission Field of Carbon Nanotube Array Microbundle. *Appl. Phys. Lett.*  
5  
6 **2018**, *112*, 013101.

7  
8  
9  
10 (10) Deshmukh, S.; Sankaran, K. J.; Srinivasu, K.; Korneychuk, S.; Banerjee, D.; Barman, A.;  
11  
12  
13  
14  
15  
16  
17  
18  
19  
20  
21  
22  
23  
24  
25  
26  
27  
28  
29  
30  
31  
32  
33  
34  
35  
36  
37  
38  
39  
40  
41  
42  
43  
44  
45  
46  
47  
48  
49  
50  
51  
52  
53  
54  
55  
56  
57  
58  
59  
60  
Bhattacharya, G.; Phase, D. M.; Gupta, M.; Verbeeck, J.; Leou, K. C.; Lin, I. N.; Haenen, K.;  
Roy, S. S. Local Probing of the Enhanced Field Electron Emission of Vertically Aligned  
Nitrogen-doped Diamond Nanorods and Their Plasma Illumination Properties. *Diamond Relat.*  
*Mater.* **2018**, *83*, 118–125.

(11) Zhou, S.; Chen, K.; Cole, M. T.; Li, Z.; Chen, J.; Li, C.; Dai, Q. Ultrafast Field Emission  
Electron Sources Based on Nanomaterials. *Adv. Mater.* **2019**, 1805845.

(12) Giubileo, F.; Bartolomeo, A. D.; Iemmo, L.; Luongo, G.; Urban, F. Field Emission from  
Carbon Nanostructures. *Appl. Sci.* **2018**, *8*, 526.

(13) Sankaran, K. J.; Srinivasu, K.; Leou, K. C.; Tai, N. H.; Lin, I. N. High Stability Electron  
Field Emitters Made of Nanocrystalline Diamond Coated Carbon Nanotubes. *Appl. Phys. Lett.*  
**2013**, *103*, 251601.

(14) Chang, T.; Lu, F.; Kunuku, S.; Leou, K.; Tai, N.; Lin, I. Enhanced Electron Field  
Emission Properties from Hybrid Nanostructures of Graphene/Si Tip Array. *RSC Adv.* **2015**, *5*,  
2928–2933.

(15) Varshney, D.; Rao, C. V.; Mendoza, F.; Perez, K.; Guinel, M. J.-F.; Ishikawa, Y.;  
Weiner, B. R.; Morell, G. Electron Emission of Graphene-Diamond Hybrid Films Using Paraffin  
Wax as Diamond Seeding Source. *World J. Nano Sci. Engg.* **2012**, *2*, 126–133.

(16) Chang, I. L.; Tsai, P. H.; Tsai, H. Y. Field Emission Characteristics of CNFB-CNT  
Hybrid Material Grown by One-step MPCVD. *Diamond Relat. Mater.* **2016**, *69*, 229–236.

1  
2  
3 (17) Tsai, P. H.; Tsai, H. Y. Fabrication and Field Emission Characteristic of Microcrystalline  
4 Diamond/Carbon Nanotube Double Layered Pyramid Arrays. *Thin Solid Films* **2015**, *584*,  
5 330–335.  
6  
7  
8  
9

10 (18) Chang, T. H.; Hsieh, P. Y.; Kunuku, S.; Lou, S. C.; Manoharan, D.; Leou, K. C.; Lin, I.  
11 N. ; Tai, N. H. High Stability Electron Field Emitters Synthesized via The Combination of  
12 Carbon Nanotubes and N<sub>2</sub>-Plasma Grown Ultrananocrystalline Diamond Films. *ACS Appl.*  
13 *Mater. Interfaces* **2015**, *7*, 27526–27538.  
14  
15  
16  
17  
18

19 (19) Yuge, R.; Miyawaki, J.; Ichihashi, T.; Kuroshima, S.; Yoshitake, T.; Ohkawa, T.; Aoki,  
20 Y.; Iijima, S.; Yudasaka, M. Highly Efficient Field Emission from Carbon Nanotube-Nanohorn  
21 Hybrids Prepared by Chemical Vapor Deposition. *ACS Nano* **2010**, *12*, 7337–7343.  
22  
23  
24  
25

26 (20) Dai, W.; Chung, C. Y.; Alam, F. E.; Hung, T. T.; Sun, H.; Wei, Q.; Lin, C. T.; Chen, S.  
27 K.; Chin, T. S. Superior Field Emission Performance of Graphene/Carbon Nanofilament  
28 Hybrids Synthesized by Electrochemical Self-exfoliation. *Mater. Lett.* **2017**, *205*, 223–225.  
29  
30  
31  
32

33 (21) Xiao, X.; Auciello, O.; Cui, H.; Lowndes, D. H.; Merkulov, V. L.; Carlisle, J. Synthesis  
34 and Field Emission Properties of Hybrid Structures of Ultrananocrystalline Diamond and  
35 Vertically Aligned Carbon Nanofibers. *Diamond Relat. Mater.* **2006**, *15*, 244–247.  
36  
37  
38  
39

40 (22) Zou, Y.; May, P. W.; Vieira, S. M. C.; Fox, N. A. Field Emission from Diamond-Coated  
41 Multiwalled Carbon Nanotube “teepee” Structures. *J. Appl. Phys.* **2012**, *112*, 044903.  
42  
43  
44

45 (23) Zanin, H.; May, P. W.; Hamanaka, M. H. M. O.; Corat, E. J. Field Emission from Hybrid  
46 Diamond-like Carbon and Carbon Nanotube Composite Structures. *ACS Appl. Mater. Interfaces*  
47 **2013**, *5*, 12238–12243.  
48  
49  
50  
51  
52  
53  
54  
55  
56

1  
2  
3 (24) Uppireddi, K.; Weiner, B. R.; Morell, G. Field Emission Stability and Properties of  
4 Simultaneously Grown Microcrystalline Diamond and Carbon Nanostructure Films. *J. Vac. Sci.*  
5 *Tech. B* **2010**, *28*, 1202–1205.

6  
7  
8  
9  
10 (25) Koh, A. T. T.; Chen, T.; Pan, L.; Sun, Z.; Chua, D. H. C. Effective Hybrid  
11 Graphene/Carbon Nanotubes Field Emitters by Electrophoretic Deposition. *J. Appl. Phys.* **2013**,  
12 *113*, 174909.

13  
14  
15 (26) Liu, J.; Zeng, B.; Wang, X.; Wang, W.; Shi, H. One-step Growth of Vertical Graphene  
16 Sheets on Carbon Nanotubes and Their Field Emission Properties. *Appl. Phys. Lett.* **2013**, *103*,  
17 053105.

18  
19 (27) Nguyen, D. D.; Lai, Y. T.; Tai, N. H. Enhanced Field Emission Properties of a Reduced  
20 Graphene oxide/Carbon Nanotube Hybrid Film. *Diamond Relat. Mater.* **2014**, *47*, 1–6.

21  
22 (28) Sankaran, K. J.; Yeh, C. J.; Drijkoningen, S.; Pobedinskas, P.; Van Bael, M. K.; Leou, K.  
23 C.; Lin, I. N.; Haenen, K. Enhancement of Plasma Illumination Characteristics of Few-layer  
24 Graphene Diamond Nanorods Hybrid. *Nanotechnology* **2017**, *28*, 065701.

25  
26 (29) Piazza, F.; Golanski, A.; Schulze, S.; Relihan, G. Transpolyacetylene Chains in  
27 Hydrogenated Amorphous Carbon Films Free of Nanocrystalline Diamond. *Appl. Phys. Lett.*  
28 **2003**, *82*, 358–360.

29  
30 (30) Nemanich, R. J.; Solin, S. A. First- and Second-order Raman Scattering from Finite-size  
31 Crystals of Graphite. *Phys. Rev. B* **1979**, *20*, 392–401.

32  
33 (31) Bokobza, L.; Zhang, J. Raman Spectroscopic Characterization of Multiwall Carbon  
34 Nanotubes and of Composites. *Express Polym. Lett.* **2012**, *6*, 601–608.

1  
2  
3 (32) Sobaszek, M.; Siuzdak, K.; Ryl, J.; Sawczak, M.; Gupta, S.; Carrizosa, S. B.; Ficek,  
4 M.; Dec, B.; Darowicki, K.; Bogdanowicz, R. Diamond Phase ( $sp^3$ -C) Rich Boron-Doped  
5 Carbon Nanowalls ( $sp^2$ -C): Physicochemical and Electrochemical Properties. *J. Phys. Chem.*  
6  
7  
8  
9  
10 C. **2017**, *121*, 20821–20833.

11  
12  
13 (33) Veetil, M. K. K.; Gamache, R. M.; Bernstein, N.; Goswami, R.; Qadri, S. B.; Fears, K.  
14 P.; Miller, J. B.; Glaser, E. R.; Keller, T. M. Substitution of Silicon Within the Rhombohedral  
15 Boron Carbide ( $B_4C$ ) Crystal Lattice Through High-Energy Ball Milling. *J. Mater. Chem. C.*  
16  
17  
18  
19  
20 **2015**, *3*, 11705–11716.

21  
22  
23 (34) Wang, K.; Kang, X.; Kang, Q.; Zhong, Y.; Hu, C.; Wang, P. Improved Reversible  
24 Dehydrogenation of 2LiBH<sub>4</sub>-MgH<sub>2</sub> Composite by the Controlled Formation of Transition Metal  
25 Boride. *J. Mater. Chem. A.* **2014**, *2*, 2146–2151.

26  
27  
28  
29  
30  
31 (35) Cermignani, W.; Paulson, T. E.; Onneby, C.; Pantano, C. G. Synthesis and  
32 Characterization of Boron-doped Carbons. *Carbon* **1995**, *33*, 367–374.

33  
34  
35  
36 (36) Siuzdak, K.; Ficek, M.; Sobaszek, M.; Ryl, J.; Gnyba, M.; Niedzialkowski, P.;  
37 Malinowska, N.; Karczewski, J.; Bogdanowicz, R. Boron-Enhanced Growth of Micron-Scale  
38 Carbon-Based Nanowalls: A Route Toward High Rates of Electrochemical Biosensing. *ACS*  
39  
40  
41  
42  
43 *Appl. Mater. Interfaces* **2017**, *9*, 12982–12992.

44  
45  
46 (37) Chaudhari, N. K.; Song, M. Y.; Yu, J. S. Heteroatom-doped Highly Porous Carbon from  
47 Human Urine. *Sci. Rep.* **2014**, *4*, 5221.

(38) Yang, J.; Xu, M.; Wang, J.; Jin, S.; Tan, B. A Facile Approach to Prepare Multiple Heteroatom-Doped Carbon Materials from Imine-Linked Porous Organic Polymers. *Sci. Rep.* **2018**, *8*, 4200.

(39) Sankaran, K. J.; Ficek, M.; Kunuku, S.; Panda, K.; Yeh, C. J.; Park, J. Y.; Sawczak, M.; Michałowski, P. P.; Leou, K. C.; Bogdanowicz, R.; Lin, I. N.; Haenen, K. Self-organized Multi-layered Graphene-Boron Doped Diamond Hybrid Nanowalls for High-Performance Electron Emission Devices. *Nanoscale* **2018**, *10*, 1345–1355.

(40) Chubenko, O.; Baturin, S. S.; Baryshev, S. V. Scanning Probe Microscopy and Field Emission Schemes for Studying Electron Emission from Polycrystalline Diamond. *Appl. Phys. Lett.* **2016**, *109*, 113102.

(41) Wisitsoraat, A.; Kang, W. P.; Davidson, J. L.; Li, Q.; Xu, J. F.; Kerns, D. V. Efficient Electron Emitter Utilizing Boron-doped Diamond Tips with  $sp^2$  Content. *Appl. Surf. Sci.* **1999**, *146*, 280–286.

(42) Kwon, S. J.; Shin, Y. H.; Asalm, D. M.; Lee, J. D. Field Emission Properties of the Polycrystalline Diamond Film Prepared by Microwave-Assisted Plasma Chemical Vapor Deposition. *J. Vac., Sci. Technol. B* **1998**, *16*, 712–715.

(43) Lee, Y. C.; Lin, S. J.; Lin, I. N.; Cheng, H. F. Effect of Boron Doping on the Electron-Field-Emission Properties of Nanodiamond Films. *J. Appl. Phys.* **2005**, *97*, 054310.

(44) Panda, K.; Jeong, J. H.; Park, J. Y.; Sankaran, K. J.; Sundaravel, B.; Lin, I. N. Nanoscale Investigation of Enhanced Electron Field Emission for Silver Ion Implanted/Post-annealed Ultrananocrystalline Diamond Films. *Sci. Rep.* **2017**, *7*, 16325.

(45) Mariotti, D.; Ostrikov, K. Tailoring Microplasma Nanofabrication: From Nanostructures to Nanoarchitectures. *J. Phys. D: Appl. Phys.* **2009**, *42*, 092002.

1  
2  
3 (46) Schoenbach, K. H.; Becker, K. 20 years of Microplasma Research: A Status Report. *Eur.*  
4  
5 *Phys. J. D* **2016**, *70*, 29.

6  
7  
8 (47) Ostrikov, K. Control of Energy and Matter at Nanoscales: Challenges and Opportunities  
9  
10 for Plasma Nanoscience in a Sustainability Age. *J. Phys. D: Appl. Phys.* **2011**, *44*, 174003.

11  
12 (48) Barezzi, N.; Laroussi, M. Effect of Low Temperature Plasmas on Cancer Cells. *Plasma*  
13  
14 *Process. Polym.* **2013**, *10*, 1039–1050.

15  
16 (49) Saravanan, A.; Huang, B. R.; Manoharan, D.; Lin, I. N. High-Performance Electron Field  
17  
18 Emitters and Microplasma Cathodes Based on Conductive Hybrid Granular Structured Diamond  
19  
20 Materials. *ACS Appl. Mater. Interfaces* **2017**, *9*, 4916–4925.

21  
22 (50) Venkatraman, V.; Garg, A.; Peroulis, D. Direct Measurements and Numerical  
23  
24 Simulations of Gas Charging in Microelectromechanical System Capacitive Switches. *Appl.*  
25  
26 *Phys. Lett.* **2012**, *100*, 083503.

27  
28 (51) Kalita, G.; Wakita, K.; Umeno, M. Low Temperature Growth of Graphene Film by  
29  
30 Microwave Assisted Surface Wave Plasma CVD for Transparent Electrode Application. *RSC*  
31  
32 *Adv.* **2012**, *2*, 2815–2820.

33  
34 (52) Kovarik, P.; Bourdon, E. B. D.; Prince, R. H. Electron-Energy-Loss Characterization of  
35  
36 Laser-Deposited a-C, a-C:H, and Diamond Films. *Phys. Rev. B:Condens. Matter* **1993**, *48*,  
37  
38 12123.

39  
40 (53) Prawer, S.; Peng, J. L.; Orwa, J. O.; McCallum, J. C.; Jamieson, D. N.; Bursill, L. A. Size  
41  
42 Dependence of Structural Stability in Nanocrystalline Diamond. *Phys. Rev. B: Condens.Matter*  
43  
44 **2000**, *62*, R16360.

1  
2  
3 (54) Kurian, J.; Sankaran, K. J.; Thomas, J. P.; Tai, N. H.; Chen, H. C.; Lin, I. N. The Role of  
4 Nanographitic Phase on Enhancing the Electron Field Emission Properties of Hybrid Granular  
5 Structured Diamond Films: The Electron Energy Loss Spectroscopic Studies. *J. Phys. D: Appl.*  
6 *Phys.* **2014**, *47*, 415303.

7  
8  
9  
10  
11  
12 (55) Hirai, H.; Kondo, K. Modified Phases of Diamond Formed Under Shock Compression  
13 and Rapid Quenching. *Science* **1991**, *253*, 772–774.

14  
15  
16  
17 (56) Sankaran, K. J.; Kumar, N.; Kurian, J.; Ramadoss, R.; Chen, H. C.; Dash, S.; Tyagi, A.  
18 K.; Lee, C. Y.; Tai, N. H.; Lin, I. N. Improvement in Tribological Properties by Modification of  
19 Grain Boundary and Microstructure of Ultrananocrystalline Diamond Films. *ACS Appl. Mater.*  
20 *Interfaces* **2013**, *5*, 3614–3624.

21  
22  
23  
24  
25  
26  
27 (57) Sankaran, K. J.; Huang, B. R.; Saravanan, A.; Manoharan, D.; Tai, N. H.; Lin, I. N.  
28 Nitrogen-Incorporated Ultrananocrystalline Diamond Microstructures From Bias-Enhanced  
29 Microwave N<sub>2</sub>/CH<sub>4</sub>-Plasma Chemical Vapor Deposition. *Plasma Process. Polym.* **2016**, *13*, 419.

30  
31  
32  
33  
34  
35 (58) Saravanan, A.; Huang, B. R.; Sankaran, K. J.; Kunuku, S.; Dong, C. L.; Leou, K. C.; Tai,  
36 N. H.; Lin, I. N. Bias-enhanced Nucleation and Growth Processes for Ultrananocrystalline  
37 Diamond Films in Ar/CH<sub>4</sub> Plasma and Their Enhanced Plasma Illumination Properties. *ACS*  
38 *Appl. Mater. Interfaces* **2014**, *6*, 10566–10575.

39  
40  
41  
42  
43  
44 (59) Butler, J. E.; Oleynik, I. A Mechanism for Crystal Twinning in the Growth of Diamond  
45 by Chemical Vapor Deposition. *Philos. Trans. R. Soc. Lond. Math. Phys. Eng. Sci.* **2008**, *366*,  
46  
47  
48  
49  
50  
51 295.

52  
53 (60) Bogdanowicz, R.; Sobaszek, M.; Ryl, J.; Gnyba, M.; Ficek, M.; Golunski, L.; Bock, W.  
54 J.; Smietana, M.; Darowicki, K. Improved Surface Coverage of an Optical Fibre with  
55



1  
2  
3 Nanocrystalline Diamond by the Application of Dip-coating Seeding. *Diamond Relat. Mater.*  
4  
5 **2015**, 55, 52–63.  
6  
7  
8  
9  
10  
11  
12  
13  
14  
15  
16  
17  
18  
19  
20  
21  
22  
23  
24  
25  
26  
27  
28  
29  
30  
31  
32  
33  
34  
35  
36  
37  
38  
39  
40  
41  
42  
43  
44  
45  
46  
47  
48  
49  
50  
51  
52  
53  
54  
55  
56  
57  
58  
59  
60

## Graphical Abstract

